J. Fluid Mech. (2002), *vol.* 450, *pp.* 207–233.
DOI: 10.1017/S0022112001006449 Printed in the United Kingdom

Oscillating structures in a stretched–compressed vortex

By MALEK ABID[1], BRUNO ANDREOTTI[2], STÉPHANE DOUADY[2] AND CAROLINE NORE[3]

[1]Institut de Recherche sur les Phénomènes Hors Equilibre, UMR CNRS et Université d'Aix-Marseille I, 49 Rue Joliot Curie, BP 146, 13384 Marseille Cedex 13, France

[2]Laboratoire de Physique Statistique de l'Ecole Normale Supérieure associé au CNRS et aux Universités Paris 6 et 7, 24 rue Lhomond, 75231 Paris Cedex 05, France

[3]Université Paris XI, Laboratoire d'Informatique pour la Mécanique et les Sciences de l'Ingénieur, CNRS, BP 133, 91403 Orsay Cedex, France

(Received 29 July 1999 and in revised form 3 May 2001)

The dynamics of a vortex subject to a localized stretching is numerically investigated. The structure of the flow is analysed in the case of an initially two-dimensional vortex surrounded by a periodic array of vortex rings localized far from its core. Amplified oscillations of both the axial vorticity and the stretching are found, in strong contrast with Burgers-like vortices. The resulting dynamics is the appearance, around the vortex, of successive vortical structures of smaller and smaller radius and alternate sign embedded in the previous vortical rings. The frequency scaling of the oscillations is recovered by linear analysis (Kelvin modes) but not the amplification nor the shape of the successive tori. An inviscid model based on structures is presented, which compares better with the numerical computations. These results suggest that the formalism of Kelvin waves is not sufficient to describe the full dynamics, which is instead related to the feedback of rotation on stretching and more conveniently described in terms of localized structures. We finally discuss the relative timescales of vortex stretching and of vortex reaction. The Burgers-like vortices, where there is no such reaction, turn out to correspond to a nearly pure strain field, slightly disturbed by rotation.

1. Introduction

Vortices have always been a subject of much fascination to fluid dynamicists. The variety of motions possible in such simple structures is remarkable: they can merge, intensify, reconnect, break down or give rise to waves. Recently, interest in vortex dynamics has been renewed by observations of tube-like high-vorticity regions in both simulated (Siggia 1981; Brachet *et al.* 1983; Hussain 1986; Brachet 1990; Jimenez *et al.* 1993; Kerr & Dold 1994) and real turbulent flows (Douady, Couder & Brachet 1991; Cadot, Douady & Couder 1995). Experimentally, correlations between flow visualizations using air bubbles (Cadot *et al.* 1995) and local measurements of pressure and velocity have lead to an individual characterization of large-scale vortices (filaments); the detection of large strain regions on one-point velocity signals (Belin *et al.* 1996) has been used to investigate the characteristics of the small-scale vortices (worms) present in turbulent flows. Numerically, several methods have been developed to identify (Jeong & Hussain 1995; Miura & Kida 1997) and characterize

coherent structures, showing for instance that the worm radii are most often of the order of the Kolmogorov dissipation lengthscale (Jimenez *et al.* 1993). If it is clear that there exist some strongly rotating regions in turbulent flows, many questions remain concerning, for example, their degree of coherence compared to the turbulent background (Jimenez & Wray 1994), the role they play in turbulence dynamics (Tsinober 1998) and the existence of a continuous distribution of such 'structures', both in scale and in amplitude. If the importance of vortices for turbulence has not been proved so far, vortex dynamics nonetheless remains the favoured field of investigation for the understanding of basic hydrodynamical mechanisms.

The first natural step in the investigation of vortical flows was to understand the dynamics of a single isolated vortical structure. This has lead to a large number of studies starting from crude models of filament motion computed by the Biot-Savart law or by its regularized version, called the local induction approximation (Da Rios 1906; Hasimoto 1972; Ricca 1994 and references therein), to more realistic ones used to describe vortex instabilities (Saffman 1992; Abid & Brachet 1998), and wave motion on vortex cores (Kelvin 1880; Maxworthy, Hopfinger & Redekopp 1985; Hopfinger 1992; Leonard 1994; Arendt, Fritts & Andreassen 1997) etc. It turns out that the dynamics of isolated nearly tubular vortices is dominated by the propagation of waves (Kelvin 1880) guided by their core. Among these studies, Melander & Hussain (1994) have recently investigated decaying core area variations of an axisymmetric vortex column with no external shear. Later, Schoppa, Hussain & Metcalfe (1995) focused on vortex core dynamics during primary and secondary instabilities of a plane mixing layer. They have shown the existence of vortex core oscillatory modes coupled to a meridional flow. This coupling results in an outward ejection of roll core fluid and in the creation of a localized small-scale stretched vortex sheath.

To take into account the effect of the surrounding flow, vortical structures submitted to an imposed external stretching were investigated. Indeed, as was first noted by Taylor (1938), the amplification of rotation by stretching is one of the most important mechanisms acting in fluid dynamics. For instance, the existence of a turbulent energy cascade from large to small scales can be related to the predominance, on the average, of vortex stretching over vortex compression (see Ohkitani & Kishiba 1995; Andreotti, Douady & Couder 1997; Tsinober 1998; Andreotti 1999 and references therein). More directly, vortex stretching is responsible for the intensification of vortices. The most well-known model of stretched vortex is an exact solution of the Navier–Stokes equations due to Burgers (1940). In this model, the stretching γ is constant, both spatially and temporally, and corresponds to the meridional velocity:

$$v_r = -\tfrac{1}{2}\gamma r, \quad v_z = \gamma z.$$

The evolution of the vortex is governed by the competition between vortex stretching and viscous diffusion. In the stationary regime, the azimuthal velocity is

$$v_\theta = \frac{\Gamma}{r}\left(1 - \exp\left(-\frac{r^2}{R^2}\right)\right), \tag{1.1}$$

where R is the vortex core radius and $2\pi\Gamma$ the velocity circulation. This radius R results from a balance between stretching and viscous diffusion. The particularity of this solution and more generally of all the Burgers-like models is that the stretching field is imposed and thus does not evolve. Belonging to this class of solutions is the generalization of the Burgers vortex to an elliptical vortex by Moffatt, Kida & Ohkitani (1994) and its stability has been investigated by Le Dizès, Rossi & Moffatt (1996). These authors showed that a stretched vortex can survive even when two of the

principal rates of strain are positive. Other examples of such stretched structures have been found by Neu (1984), Craik & Criminale (1986) and Kerr & Dold (1994). In these analytical works, the stretching is not only permanent but also spatially uniform.

A different kind of Burgers-like model has been proposed by Sullivan (1959) and Donaldson & Sullivan (1960), who have studied structures stretched by vorticity regions spatially localized but imposed as previously. They prescribed an axial velocity of the form $v_z = \gamma(r)z$ and have found a class of steady solutions of the Navier–Stokes equations in which there is no feedback of the vortex (v_θ) on the stretching $\gamma(r)$. The stretching is thus only subjected to its own action and to the viscous diffusion. These solutions have been extended to the unsteady case by Bellamy-Knights (1970) and more recently by Gibbon, Focas & Doering (1999) who have added an axial jet to the vortex ($v_z = \gamma(r,t)z + W(r,\theta,t)$). Again, the stretching $\gamma(r,t)$ evolves under its own action and is controlled by a boundary condition on the pressure Hessian at infinity. It turns out that the axial jet W is damped where the vortex v_θ is stretched and amplified where the vortex is compressed. Similarly, Verzicco, Jimenez & Orlandi (1995) have numerically analysed the dynamics of vortices subject to a non-uniform imposed axial strain whose spatial average is null. They found that the vortex can even survive a strong axial compression. In their numerical simulations, an axisymmetric vortical steady state is reached after emission of axial Kelvin waves damped by viscosity. As in Melander & Hussain (1993), they require the appearance of a separation bubble inside the vortex where the vorticity is decreased and the strain rate increased, around compressive stagnation points. That study was completed by Marshall (1997) who demonstrated the ejection of axial vorticity at a compressive stagnation point, together with the emission of Kelvin waves on the columnar vortex.

However, in real flows, vortices and more generally regions exhibiting rotation are neither isolated nor subjected to an imposed straining field. Our aim is to investigate a more complex situation where both the vortex and the stretching evolve freely. What occurs if a vortex is subject to stretching due to a localized structure and thus not fixed nor uniform? Is there, as suggested by recent experiments (Andreotti *et al.* 1997; Andreotti 1999), a feedback of the vortex on the stretching?

The evolution in time of the vorticity ω_i is governed by the equation

$$\partial_t \omega_i + v_j \partial_j \omega_i = \sigma_{ij}\omega_j + \nu \partial_j \partial_j \omega_i, \tag{1.2}$$

where $\sigma_{ij} = (\partial_i v_j + \partial_j v_i)/2$ is the strain tensor and ν the kinematic viscosity. The vortex stretching corresponds to the action of the strain σ_{ij} on vorticity ω_i. The strain tensor equation is

$$\partial_t \sigma_{ij} + v_j \partial_j \sigma_{ij} = \tfrac{1}{4}(\omega_k\omega_k\delta_{ij} - \omega_i\omega_j) - \sigma_{ik}\sigma_{kj} - \Pi_{ij} + \nu \partial_j \partial_j \sigma_{ij}, \tag{1.3}$$

where $\Pi_{ij} = \partial_{ij} p$ is the pressure Hessian. The strain is not only advected and damped by viscosity but also evolves under the complicated effects of vorticity, strain and pressure. It is crucial to note that (1.3) is a non-local equation (Ohkitani & Kishiba 1995) since pressure depends on the whole flow (in particular on boundary conditions) through the Poisson equation:

$$\Pi_{ii} = \tfrac{1}{2}\omega_i\omega_i - \sigma_{ij}\sigma_{ij}. \tag{1.4}$$

Obviously the dynamics of strain depends on the particular physical situation through pressure non-locality. Nevertheless, one can ask whether some robust mechanisms can be identified under the dynamics of stretching.

In this paper, we numerically study a simple particular case where a vortex is subjected to a spatially periodic stretching–compression due to an array of localized

Run	a	b	c	d	e	f	g	h	i	j	k	l	m	n
ω_0	2.5	2.5	2.5	2.5	2.5	2.5	10	3.33	1.25	5	5	2.5	2.5	2.5
R_0	0.8	0.8	0.8	0.8	0.8	0.4	0.4	1.2	0.8	0.8	0.4	0.8	0.8	0.8
ω_1	0.1	0.1	0.1	0.2	0.4	0.1	0.1	0.1	0.1	0.1	0.1	0.1	0.1	0.1
K_z	2	0.5	1	1	1	1	1	1	1	1	1	1	1	1
ν	10^{-3}	10^{-3}	10^{-3}	10^{-3}	10^{-3}	10^{-3}	10^{-3}	10^{-3}	10^{-3}	10^{-3}	10^{-3}	10^{-5}	5×10^{-3}	10^{-2}

TABLE 1. Characteristics of the runs; they all have resolution $128 \times 128 \times 64$ except for run l for which the resolution is $160 \times 160 \times 80$.

tori. The vortical part of the flow is initially two-dimensional (i.e. not disturbed) but it is subjected to a non-uniform stretching field. Integrating the Navier–Stokes equations, the total field (both the vortex and the straining field) is let free to evolve. The next section of this paper is devoted to the description of the numerical code and of the initial conditions. The results are presented in § 3. The dynamics of the vortex and that of the stretching (both let free to evolve) appear to be very different from that of Burgers-like vortices (subjected to an imposed stretching). A parametric study accounts for the robustness of the reaction of the vortex on the stretching. This reaction is interpreted through inviscid models in § 4. We finally conclude on the mechanisms of interaction and feedback between stretching and vortices.

2. Numerical set-up

2.1. *Integration scheme*

The simulation code solves three-dimensional incompressible Navier–Stokes equations in a periodic box. The integration scheme and the spatial discretization are detailed in Abid & Brachet (1998) and only the main points are summarized here. We have chosen to use pseudo-spectral methods both for their precision and for their ease of implementation. The equations are written in Cartesian coordinates. To exactly conserve energy in the constant density inviscid limit, we use the so-called rotational formulation (Gottlieb & Orszag 1977). The temporal evolution is computed with an Adams–Bashforth Crank–Nicholson discretization scheme. For the first time step, we use a backward Euler scheme. This time-stepping scheme is globally second-order accurate in time.

In order to accommodate the vortex in a triply periodic Fourier representation, we consider a periodic array of vortices with transverse periodicity length $L_x = L_y = L$ and a longitudinal periodicity length L_z. To make the vortex profile compatible with the periodic representation, we use $r_p = (\sin^2(2\pi x/L) + \sin^2(2\pi y/L))^{1/2} L/2\pi$, instead of $r = (x^2 + y^2)^{1/2}$.

As we are interested in the dynamics of an unique stretched vortex, the planes $x = nL$, $y = mL$ are taken as fixed free-slip boundaries. The velocity field is expanded as $\boldsymbol{u}(x, y, z, t) = \sum_{k_x,k_y,k_z} (\hat{u} \sin(k_x x) \cos(k_y y), \hat{v} \cos(k_x x) \sin(k_y y), \hat{w} \cos(k_x x) \cos(k_y y)) \mathrm{e}^{\mathrm{i}k_z z}$ and projected on the space of divergence-free fields. By using these sine and cosine transformations in the lateral directions, we gain a factor of 4 in storage and number of operations for the implementation in comparison with a general periodic transform. In this periodic representation the image vortices do not induce any motion on the vortex under consideration, by symmetry. The ratio between the vortex radius and the transverse periodicity length is chosen to ensure that the vortex only diffuses, like an isolated one, when the incompressible Navier–Stokes equations are integrated.

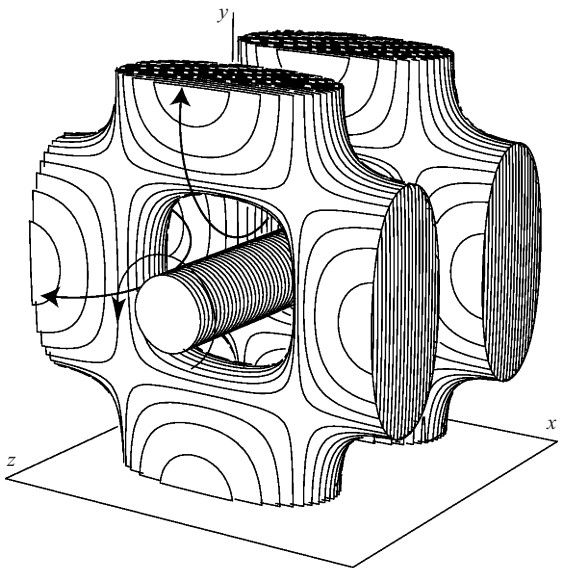

FIGURE 1. Initial condition: a Lamb's vortex is subjected to the stretching created by a periodic array of alternate rings (three-dimensional iso-surfaces $\omega_\theta = 0.075$ and $\omega_z = 1.5$). The arrows indicate the rotation of the Lamb's vortex and that of the stretching tori.

In all the runs used in table 1, the computational box is $[-\pi, \pi]^3$ (corresponding to the choice $L = 4\pi, L_z = 2\pi$) and the resolution is $128 \times 128 \times 64$ except for the run with viscosity $\nu = 10^{-5}$ for which the grid points are $160 \times 160 \times 80$. The viscosity is $\nu = 10^{-3}$ except in three cases intended to quantify the effect of viscous damping (see discussion in § 3). In all cases, the resolution was checked to be sufficient for spectral convergence.

We use two kinds of plots: a three-dimensional iso-surface of the field of interest (as in figure 1) and two-dimensional equally spaced contours in the plane $x = 0$ (as in figures 2*b* and 3*b*).

2.2. *Initial condition*

In order to investigate the interaction between a vortex and a localized stretching field, we choose an initial condition which is a superposition of a Lamb's vortex and a periodic array of alternate rings (figure 1). The Lamb's vortex (the swirling part of the flow, v_θ) is centred in the periodic box and aligned along the z-axis (see figure 2*a*, *b*), the corresponding vorticity field being

$$\omega_z = \omega_0 \exp(-r_p^2/R_0^2). \tag{2.1}$$

The vortex is characterized by two parameters: the maximal vorticity ω_0 (on its axis), and the core radius R_0. The array of rings, which creates a spatially periodic stretching–compression on the vortex axis, is defined by

$$\left.\begin{aligned} \omega_x &= -\omega_1 \cos(K_x x) \sin(K_y y) \sin(K_z z), \\ \omega_y &= \omega_1 \sin(K_x x) \cos(K_y y) \sin(K_z z), \\ \omega_z &= 0. \end{aligned}\right\} \tag{2.2}$$

This meridional flow depends on two parameters: ω_1, the maximal vorticity of the rings, and K_z the axial periodicity. Note that K_x and K_y are kept constant (equal

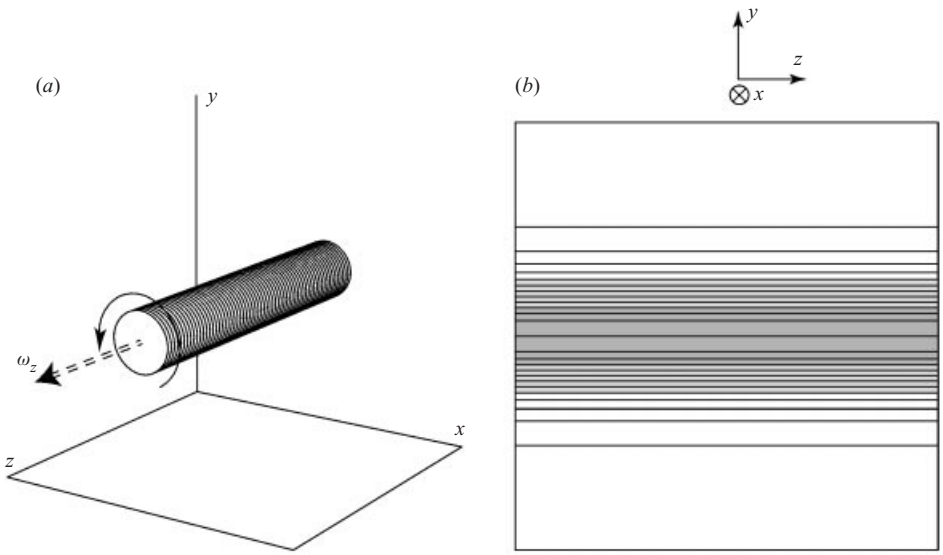

FIGURE 2. The vortex at the initial time (contours of axial vorticity ω_z). (a) Three-dimensional iso-surface ($\omega_z = 1.5$). The solid line arrow shows the rotation and the dashed one indicates the axial vorticity. (b) Two-dimensional contours in the plane $x = 0$ at equally spaced levels (0.2) from $\omega_z = 0.1$ to $\omega_z = 2.5$. The highest contour levels are shaded grey ($\omega_z \geqslant 0.9$).

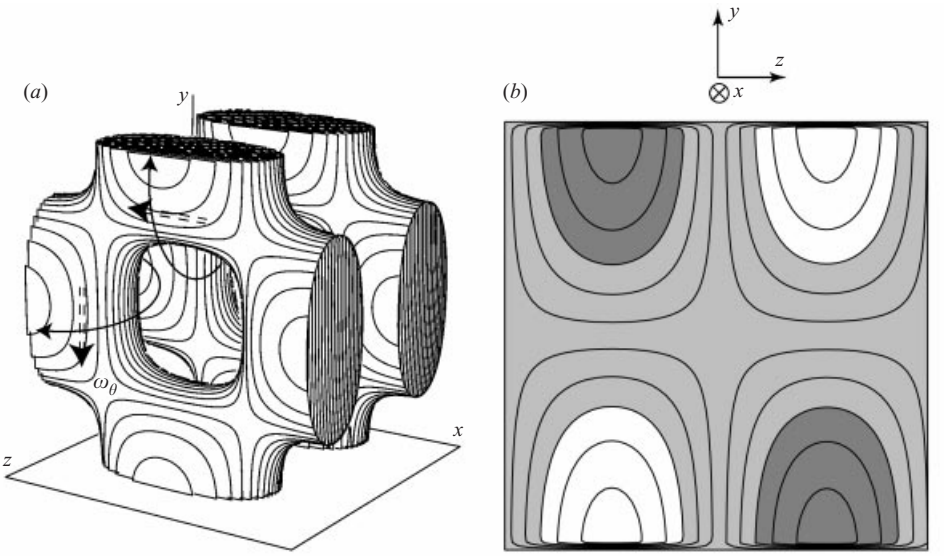

FIGURE 3. The stretching rings at the initial time (contours of azimuthal vorticity ω_θ). (a) Three-dimensional iso-surface ($\omega_\theta = 0.075$). The solid line arrows show the rotation and the dashed ones indicate the azimuthal vorticity. (b) Two-dimensional contours in the plane $x = 0$ at equally spaced levels (0.02) from $\omega_\theta = -0.1$ to $\omega_\theta = 0.1$. The positive highest contour levels are shaded dark-grey while negative lowest contour levels are white.

to 1/2) and that the ring core radius is of the order of the distance to the axis. Figure 3(b) shows the two-dimensional iso-contours of the azimuthal vorticity ω_θ at the initial time. Although not axisymmetric, the specific interest of the initial ring shape (2.2) is that their axes are located on the lateral boundaries. The stretching

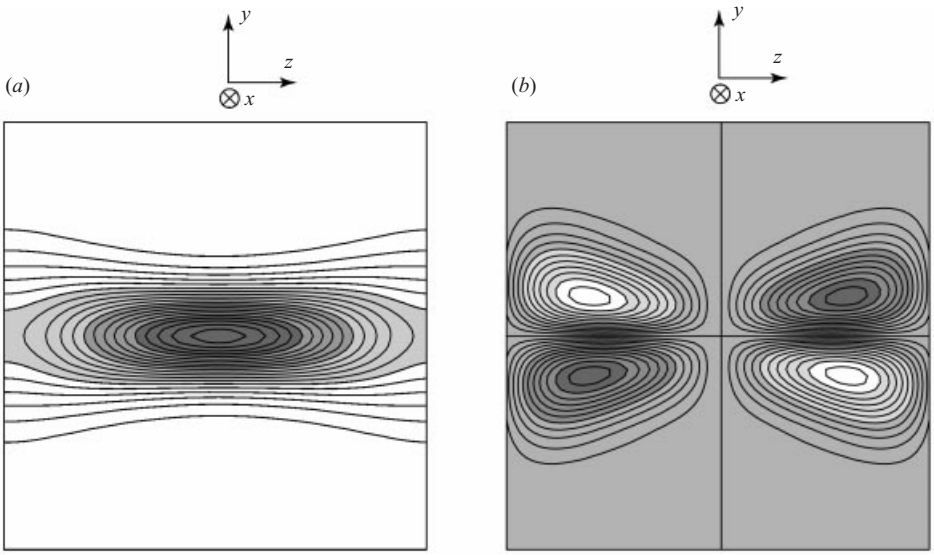

FIGURE 4. Deformation of the vortex under an imposed stretching (Burgers-like vortex). Two-dimensional contours in the plane $x = 0$ at time $t = 10$ of axial vorticity ω_z (a) and of radial vorticity ω_r (b) for the forced stretching run. The contour levels are at equally spaced levels from the minimum in white to the maximum in dark grey.

structures are thus as far as possible from the columnar vortex. It is worth noting that the vorticity has to be null on the lateral boundaries due to symmetry conditions: the rings are therefore truncated nearby.

The parameters of initial data were varied as shown in table 1. The dynamics will be described with a reference case showing generic mechanisms. The parameters of the reference run are: $\omega_0 = 2.5, R_0 = 0.8, \omega_1 = 0.1, K_z = 1$ (run c).

3. Results

3.1. *Evolution of the vortex subjected to an imposed stretching*

Before presenting the dynamics, it is interesting to examine the evolution of the vortex if the stretching is imposed, i.e. in the absence of reaction of the vortex on the rings. The numerical computation is performed by maintaining the axial velocity of the rings at its initial value and their axial vorticity at zero. To do so, we split the velocity field into two divergence-free parts $\boldsymbol{u}^{rings}$ and $\boldsymbol{u}^{vortex}$ and we impose $\omega_z^{rings} = 0$ and $u_z^{vortex} = 0$ at each time step.

Figure 4 shows the deformation of the vortex after a short time. The axial vorticity $\omega_C(t)$ at the centre of the box (C is the point $(0,0,0)$ in the box $[-\pi,\pi]^3$, thus $\omega_C(t) = \omega_z(0,0,0,t)$ and $\gamma_C(t) = \gamma(0,0,0,t)$) increases under the stretching induced by the meridional flow (figures 4a and 5a). On the other hand, at the edges, the axial vorticity decreases towards zero. The stretching remains constant by assumption (see the stretching at the centre $\gamma_C(t)$ on figure 5b). Under viscous diffusion, the vorticity saturates at long time, when the radius of the vortex core becomes of the order of the viscous scale $(\nu/\gamma)^{1/2}$ (figure 5a).

3.2. *Reaction of the vortex to the stretching*

Unlike the previous situation, when the whole flow is let free to evolve, the axial vorticity ω_C oscillates (see for comparison the inset of figure 5). The time evolution

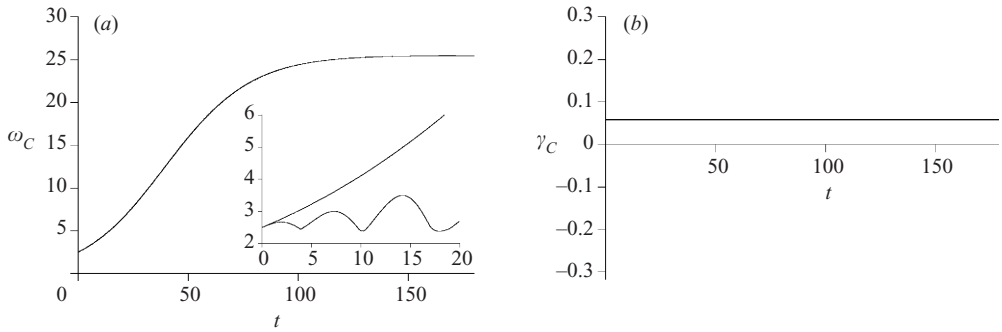

FIGURE 5. Time evolution of (a) the axial vorticity $\omega_C(t)$ and of (b) the stretching $\gamma_C(t)$ at the centre of the box for the forced stretching run. The stretching is constant by assumption so that the vorticity increases until saturation by viscous diffusion. The inset shows the first time evolution with, for comparison, the result obtained in the case where the stretching is also let free to evolve (dotted line).

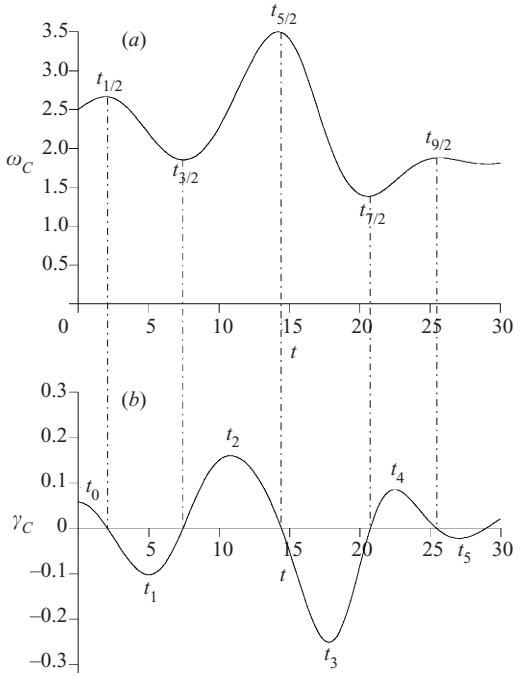

FIGURE 6. Time evolution of (a) the axial vorticity $\omega_C(t)$ and of (b) the stretching $\gamma_C(t)$ at the centre of the box for run c. The stretching oscillates in quadrature with the vorticity: contrarily to Burgers-like vortices, the vortex reacts on the stretching. See text for the definition of t_i and $t_{i/2}$.

of the axial vorticity (ω_C) and the stretching (γ_C) at the centre of the box is shown in figure 6. They appear to oscillate in quadrature. The dynamics is thus completely different from that of Burgers-like vortices. This means that there is an interaction between the vortex and the stretching rings. One can observe that the phenomenon is approximately periodic in time. We denote t_i the time of the turning point i: γ_C (figure 6b) is maximum at $t_0 = 0, t_2, t_4$, etc. and minimum at t_1, t_3, t_5, etc.; ω_C is maximum at $t_{1/2}, t_{5/2}, t_{9/2}$, etc. and minimum at $t_{3/2}, t_{7/2}$, etc. The second striking

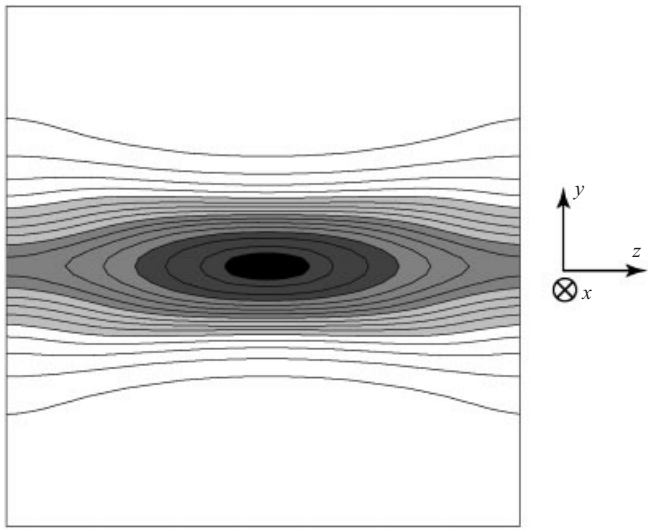

FIGURE 7. Two-dimensional contours of axial vorticity ω_z at time $t_{1/2}$ in the plane $x = 0$ at equally spaced levels from the minimum in white to the maximum in dark grey. The vortex is stretched at the box centre and compressed at the edges.

feature of the curves $\omega_C(t)$ and $\gamma_C(t)$ is the increasing amplitude of their oscillations (at least for the first turning points).

Let us examine these oscillations step by step. At short times $t < t_{1/2}$ (figure 7), the vortex core becomes thinner at the centre and thicker on the edges, as for the Burgers-like case (figure 4). This corresponds to an increasing axial vorticity at the centre under the stretching induced by the rings. On the other hand, the compression makes the core size increase at the edges. For $t > t_{1/2}$, the vorticity ω_C at the centre decreases and reaches its initial value at time t_1. At that instant, the vortex is approximately straight (as initially) and two new rings have appeared (see figure 8*a*), which rotate in the opposite way to the initial ones: more rigorously, their azimuthal vorticity is of opposite sign to that of the initial rings (figure 8*b*). Their radius is smaller and they are more axisymmetric (figure 8*c*). At that time, the initial rings have been sheared by the vortex and attenuated in their central part because of the secondary tori (figure 8*c*).

These secondary tori are induced by the differential rotation that was created by the initial rings. This can be understood with the following mechanism: at initial time t_0, the swirling part of the flow is two-dimensional. As a consequence, the pressure gradient essentially balances the centrifugal force (figure 9*a*). Let us now consider the vortex at time $t_{1/2}$ (figure 7) which rotates more rapidly at the centre of the box than at the edges. This differential rotation leads to a variation of the centrifugal force along the z-axis (figure 9*b*). This induces the creation of azimuthal vorticity (written here for the axisymmetrical case),

$$\frac{\partial \omega_\theta}{\partial t} + v_z \frac{\partial \omega_\theta}{\partial z} + r v_r \frac{\partial (\omega_\theta / r)}{\partial r} = \frac{\partial}{\partial z} \frac{v_\theta^2}{r} + \nu \left(\frac{\partial^2 \omega_\theta}{\partial z^2} + \frac{\partial}{\partial r} \left(\frac{1}{r} \frac{\partial r \omega_\theta}{\partial r} \right) \right), \tag{3.1}$$

through the source term $\partial_z(v_\theta^2/r)$. This means that the pressure gradient can no longer balance the centrifugal force. It axially varies more slowly than the centrifugal force.

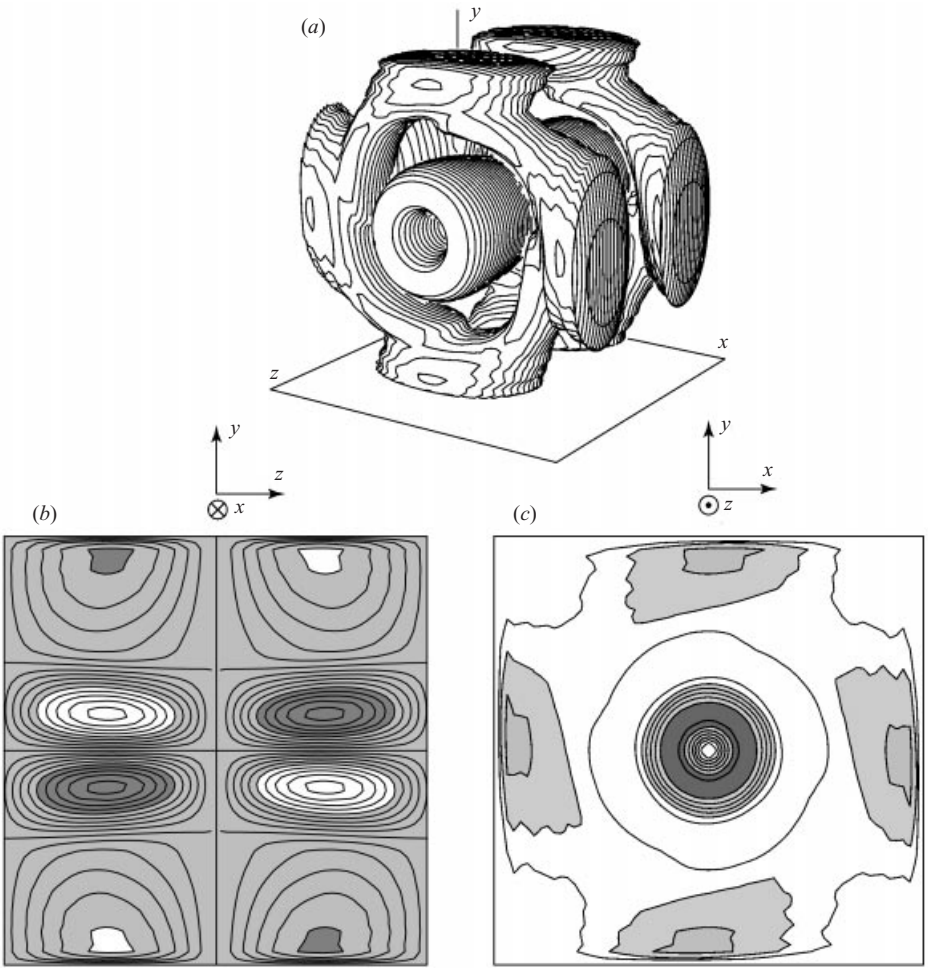

FIGURE 8. At time t_1, secondary rings have been induced inside the primary ones. (a) Three-dimensional iso-surface of the azimuthal vorticity. (b) Two-dimensional contours in the plane $x = 0$ at equally spaced levels of the component of vorticity ω_θ normal to the plane $x = 0$. Strong negative ω_θ values are represented in white and strong positive in dark grey. (c) Two-dimensional contours of the modulus of ω_θ in the plane $K_z z = \pi/2$ at equally spaced levels from the minimum in white to the maximum in dark grey.

Indeed, the induction of a radial velocity

$$\frac{\partial v_r}{\partial t} + v_r \frac{\partial v_r}{\partial r} + v_z \frac{\partial v_r}{\partial z} = \left(\frac{v_\theta^2}{r} - \frac{\partial p}{\partial r} \right) + \nu \left(\frac{\partial^2 v_r}{\partial z^2} + \frac{\partial}{\partial r} \left(\frac{1}{r} \frac{\partial r v_r}{\partial r} \right) \right) \tag{3.2}$$

is directly related to the competition between the centrifugal force v_θ^2/r and the pressure gradient $\partial_r p$. In the upper part of figure 9(b), the centrifugal force is greater than the radial pressure gradient and ejects the fluid from the axis. Reciprocally, a radial inflow appears in the lower part. As a consequence, a secondary toroidal flow is induced. This meridional flow stretches the vortex in the place where it was slowly rotating and compresses it in the region where it was rapidly rotating. The result is a negative feedback which tends to straighten the vortex.

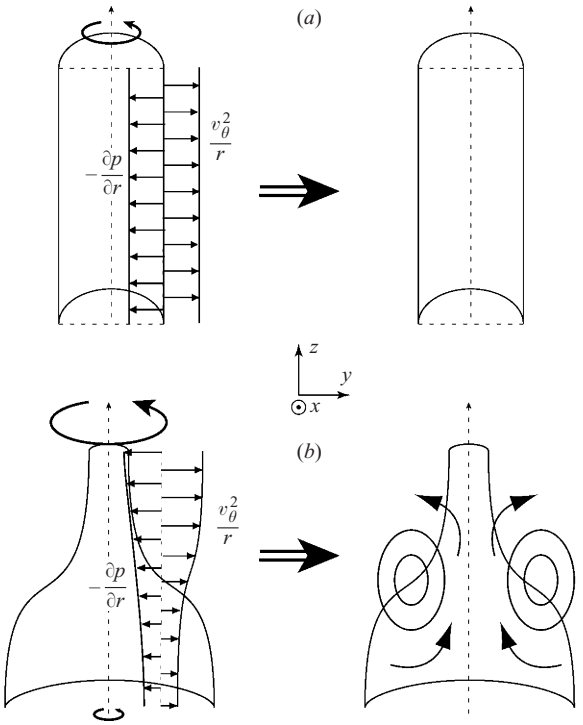

FIGURE 9. Reaction of a vortex on the stretching to which it is subjected. (*a*) In a straight vortex, the pressure gradient (left facing arrows) balances the centrifugal force (right facing arrows). (*b*) When the vortex presents a differential rotation, the pressure gradient cannot balance the centrifugal force so that a secondary flow is induced. Circular arrows indicate the axial vorticity.

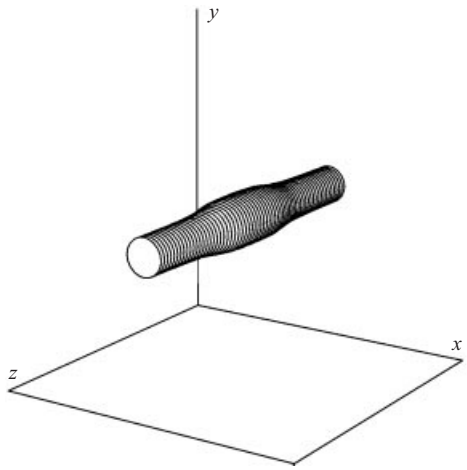

FIGURE 10. At time $t_{3/2}$, the vortex is compressed at the centre and stretched at the edges by the secondary tori. Three-dimensional iso-surface of the axial vorticity ω_z.

The secondary rings induce an axial compression so that the stretching γ_C vanishes at time $t_{1/2}$ and becomes negative thereafter. The vortex is now compressed where initially stretched and vice versa (figure 10). Again non-uniform along its axis, it induces a negative feedback to the stretching and produces some new tori inside

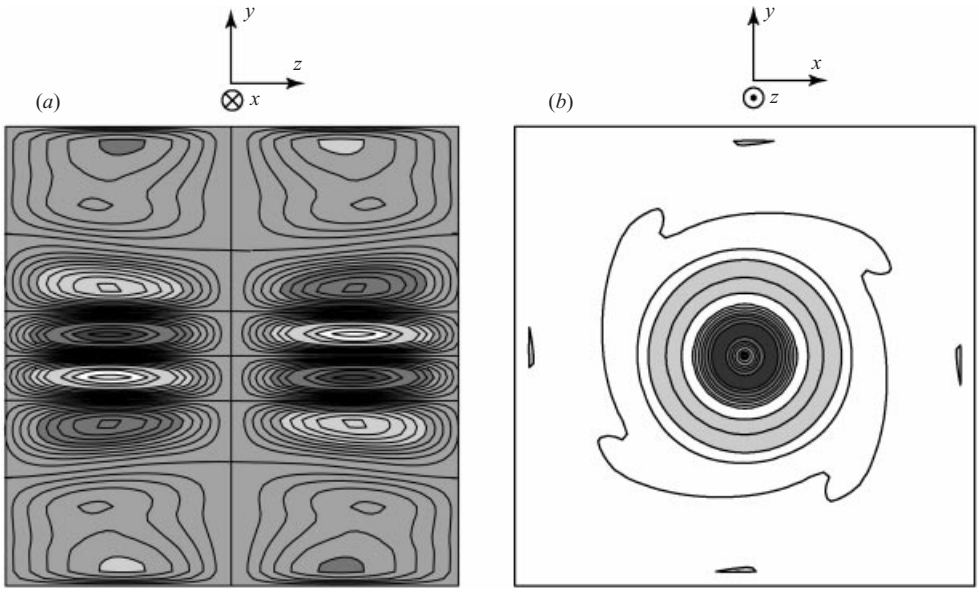

FIGURE 11. At time t_2, three generations of tori can be observed. (a) Two-dimensional contours at equally spaced levels of the component of vorticity ω_θ normal to the plane $x = 0$. Strong negative ω_x values are represented in white and strong positive in dark grey. (b) Two-dimensional contours of the modulus of ω_θ in the plane $z = \pi/2$ at equally spaced levels from the minimum in white to the maximum in dark grey.

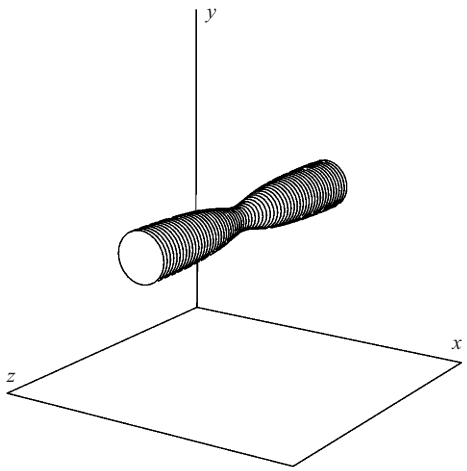

FIGURE 12. At time $t_{5/2}$, the vortex modulation is the same as at $t_{1/2}$.
Three-dimensional iso-surface of axial vorticity ω_z.

the secondary ones (figures 11a, b). This meridional flow acts like the previous one until it brings the vortex back to its initial shape (achieved at time t_2). The reaction overshoots and at time $t_{5/2}$ the vortex exhibits a strong differential rotation (figure 12) as at $t = t_{1/2}$ (figure 7). Thus the inversion of the stretching occurs again, quaternary tori being created at a smaller radius (figure 13), and so on (figure 14). On figure 15(a), we recapitulate the time evolution of the axial vorticity ω_z using its value at different locations. (C denotes the centre $(0, 0, 0)$ and B the edge $(0, 0, \pi)$ of the box $[-\pi, \pi]^3$;

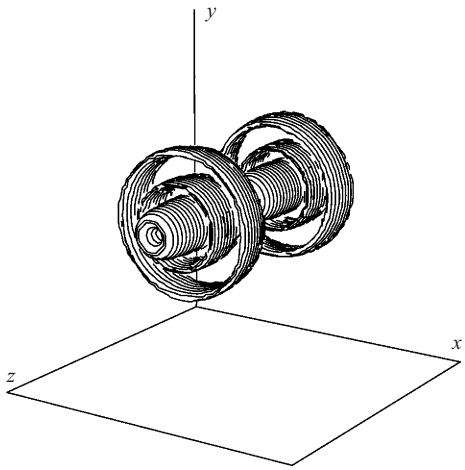

FIGURE 13. Three-dimensional iso-surface of azimuthal vorticity ω_θ at time t_3. Four generations of rings coexist but, due to the threshold used, the initial rings do not appear on the figure.

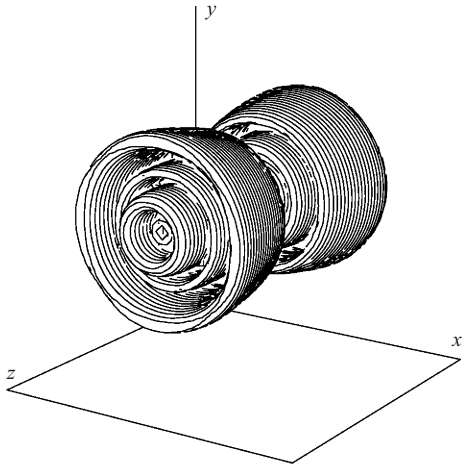

FIGURE 14. Three-dimensional iso-surface of azimuthal vorticity ω_θ. At time t_4, five generations of rings coexist. As for the previous figure, the initial rings do not appear but the fourth reaction torus can be observed at the centre.

M stands for the maximum value and m for the minimum value inside the box.) The maximum vorticity $\omega_M(t)$ is located at the centre C for $t_0 \leqslant t \leqslant t_1$ and $t_2 \leqslant t \leqslant t_3$ and at the edge B for $t_1 \leqslant t \leqslant t_2$. Figure 15($b$) shows the stretching in the same way. The quantities $\gamma_M(t)$ and $\gamma_m(t)$ are in quadrature with $\omega_M(t)$ and $\omega_m(t)$ respectively. Initially, the stretching due to the initial rings is maximum at the centre C and minimum at the edge B. The stretching γ_C initially decreases, vanishes at $t_{1/2}$ and then oscillates. The position of $\gamma_M(t)$ coincides alternately with C and B, except at larger times (dashed lines of figure 15b).

At first sight, the dynamics could be interpreted as an oscillation of the ring amplitudes. However, we instead observe (see figures 8, 11, 13, 14) the formation of successive vortex rings of smaller radius and opposite signs. To differentiate their respective effect on the stretching, we consider in figure 16 the azimuthal vorticity amplitude of the successive rings. The amplitude of the initial rings remains nearly

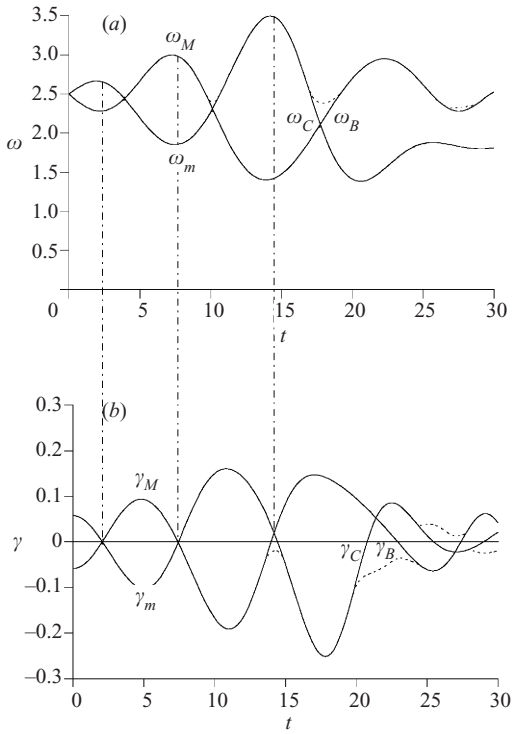

FIGURE 15. Time evolution of the axial vorticity and stretching at different locations of the box $[-\pi, \pi]^3$: (*a*) $\omega_C(t)$ (solid line), $\omega_B(t)$ (solid line), the maximum vorticity $\omega_M(t)$ (dotted line) and the minimum vorticity $\omega_m(t)$ (dotted line); (*b*) $\gamma_C(t)$ (solid line), $\gamma_B(t)$ (solid line), the maximum stretching $\gamma_M(t)$ (dotted line) and the minimum stretching $\gamma_m(t)$ (dotted line). Times $t_{i/2}$ are indicated with vertical dot-dashed lines.

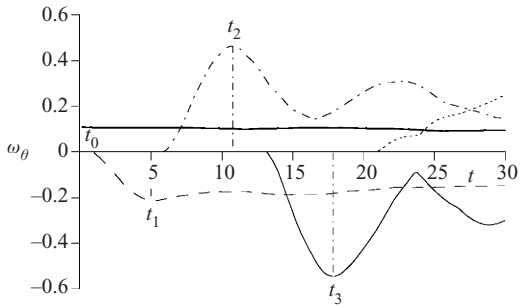

FIGURE 16. Time evolution of the azimuthal vorticity of each torus: the nearly constant initial torus (continuous line), the secondary torus (long-dashed), the tertiary torus (dot-dashed), the quaternary torus (thin continuous line) and the next one (dotted). The dynamics is not a simple oscillation in time but a superposition of the successive rings induced by the vortex.

constant in time. The first reaction rings then appear inside the vortex (figure 8*b*). Their amplitude saturates around $t = t_1$ and keeps an approximately constant value afterwards. The following oscillation of the stretching, after t_1, (figure 6*b*) is then due to the appearance of second smaller vortex rings of opposite signs (therefore of the same sign as the initial ones). The process repeats but with a slight delay after each t_i. The smaller rings have amplitudes which oscillate but never change sign. It turns

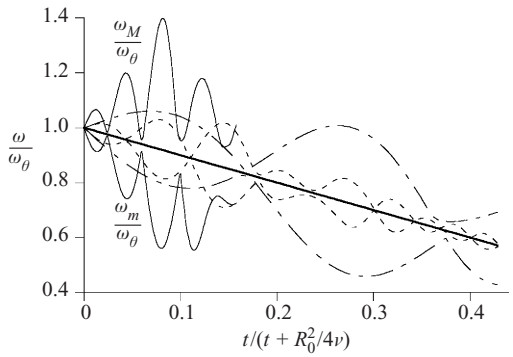

FIGURE 17. Time evolution of the rescaled maximum axial vorticity $\omega_M(t)/\omega_0$ and the minimum axial vorticity $\omega_m(t)/\omega_0$ for three different initial conditions (runs *f* (dot-dashed line), *g* (dashed line), *c* (solid line)) versus the rescaled viscous time $t/(t + R_0^2/4\nu)$. The thick solid line corresponds to the diffusion of an isolated Lamb's vortex.

out that the axial stretching simply oscillates, although created by the superposition of successive vortical structures of opposite signs.

3.3. *Scaling laws*

Another feature of figure 15(*a*) is the slow decrease of the average of ω_M and ω_m due to viscous diffusion. It can be compared to the diffusion of a Lamb's vortex whose core size R varies according to $R^2(t) = R_0^2 + 4\nu t$. By conservation of the angular momentum, the axial vorticity evolves as the inverse square of the core size as

$$\frac{\omega_L(t)}{\omega_0} = \frac{1}{1 + 4\nu t/R_0^2} = 1 - \frac{t}{t + R_0^2/4\nu}. \tag{3.3}$$

It thus decreases linearly with the rescaled viscous time $t/(t + R_0^2/4\nu)$. This viscous scaling is used to compare runs of table 1. Figure 17 shows the evolution of the rescaled maximum axial vorticity $\omega_M(t)/\omega_0$ and the minimum axial vorticity $\omega_m(t)/\omega_0$ for three different parameters sets versus the viscous time. One can observe that the curves oscillate around a line of slope -1 corresponding to the Lamb's vortex diffusion (3.3): as a first approximation, the viscous diffusion and the stretching–vortex interaction are decoupled. This means that the dynamics is dominated by the action of inertia and pressure. In order to identify the most important mechanisms, we have thus studied the flow for quite large Reynolds numbers ($\pi\omega_0 R_0^2/\nu \simeq 5 \times 10^3$ for the reference case).

Figure 18(*a*) shows the rescaled vorticities $(\omega_M(t) - \omega_L(t))K_z R_0/\gamma_0$ and $(\omega_m(t) - \omega_L(t))K_z R_0/\gamma_0$ versus the rescaled time $t(\omega_0 K_z R_0/2)$, where K_z is the wavenumber on the axis and $\gamma_0 = \gamma_C(0)$, for four different runs. These curves approximately collapse till t_2^*. At this time, the nonlinear evolution of the axial vorticity generates harmonics which reduce the quality of the collapse. Thus, at short times $t \leqslant t_2^*$, the oscillation angular frequency varies proportionally to the initial axial vorticity ω_0 multiplied by the ratio between the vortex core size R_0 and the distance $1/K_z$:

$$f \simeq 0.39\omega_0 K_z R_0. \tag{3.4}$$

At short times, the amplification rate of the axial vorticity is γ_0 which implies that

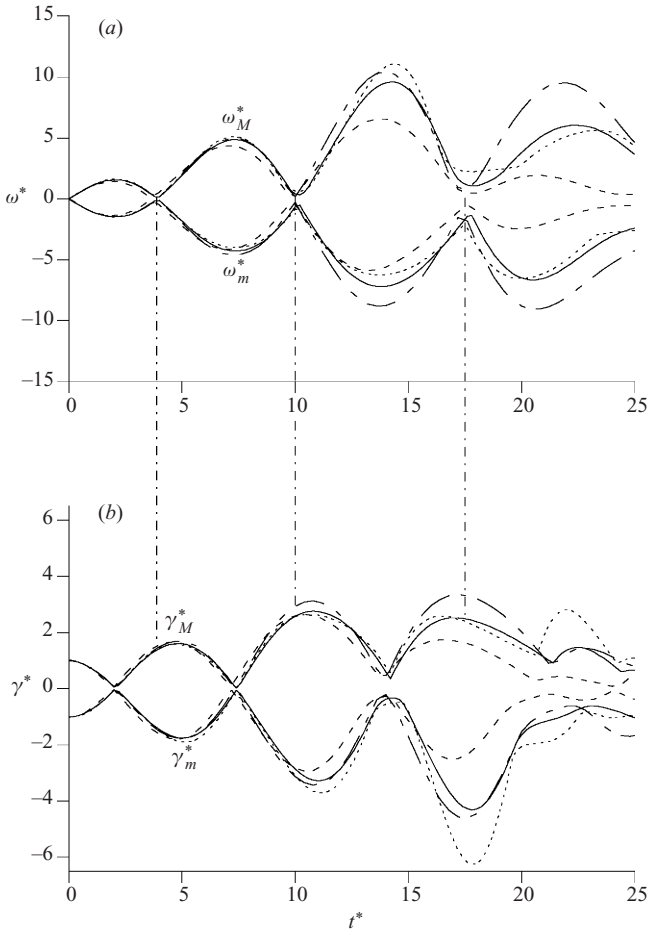

FIGURE 18. Time evolution of (*a*) the rescaled vorticities $\omega^*_M(t) = (\omega_M(t) - \omega_L(t))K_z R_0/\gamma_0$ and $\omega^*_m(t) = (\omega_m(t) - \omega_L(t))K_z R_0/\gamma_0$ and (*b*) the rescaled stretching rates $\gamma^*_M(t) = \gamma_M(t)/K_z R_0\omega_0$ and $\gamma^*_m(t) = \gamma_m(t)/K_z R_0\omega_0$ (runs *c* (solid line), *d* (dotted line), *g* (dashed line), *j* (dot-dashed line)) versus the rescaled time $t^* = t(\omega_0 R_0 K_z/2)$. Times t_i are indicated with vertical dot-dashed lines. Both the stretching and the vorticity curves collapse till t_2.

the amplitude of the oscillations is

$$\omega_M(t) - \omega_L(t) \propto \frac{\gamma_0\omega_0}{f} \propto \frac{\gamma_0}{K_z R_0}. \tag{3.5}$$

In the same way, figure 18(*b*) shows the rescaled stretching rates $\gamma^*_M(t) = \gamma_M(t)/R_0 K_z\omega_0$ and $\gamma^*_m(t) = \gamma_m(t)/R_0 K_z\omega_0$ versus the rescaled time $t^* = t(\omega_0 R_0 K_z/2)$. Again the collapse of the different curves is good till $t = t^*_2$.

Most of the runs were for the same viscosity $\nu = 10^{-3}$, but it was varied in three runs ($\nu = 10^{-5}$, $\nu = 5 \times 10^{-3}$ and $\nu = 10^{-2}$, keeping other parameters as in run *c*). As expected, when the viscosity is increased, the viscous drift of vorticity amplitudes (see figure 19) becomes more important.

The axis wavenumber K_z was also varied from 2 (run *a*) to 0.5 (run *b*) and thus the distance between the tori. As expected (see figure 20), the nearer the tori are, the faster the dynamics is.

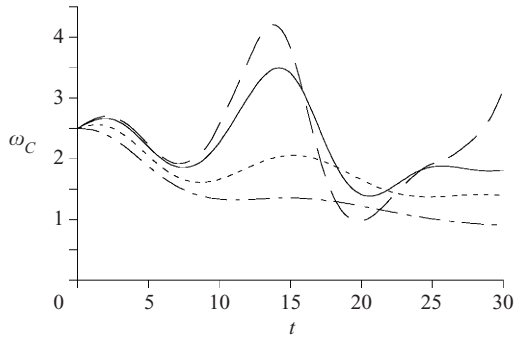

FIGURE 19. Time evolution of the axial vorticity $\omega_C(t)$ for different viscosities: for run *l*, $\nu = 10^{-5}$ (long-dashed line), run *c*, $\nu = 10^{-3}$ (solid line), run *m*, $\nu = 5 \times 10^{-3}$ (dotted line) and run *n*, $\nu = 10^{-2}$ (dot-dashed line).

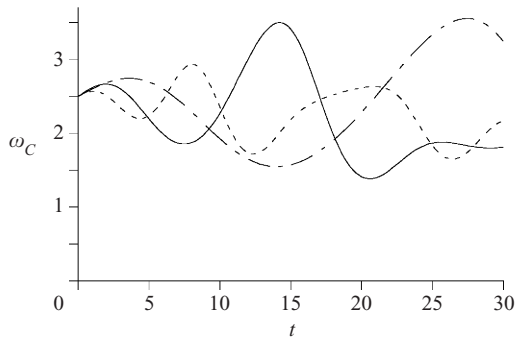

FIGURE 20. Time evolution of the axial vorticity $\omega_C(t)$ for different axis wavenumbers K_z: for run *c*, $K_z = 1$ (solid line), run *a*, $K_z = 2$ (dotted line) and run *b*, $K_z = 0.5$ (dot-dashed line).

4. Inviscid modelling of the vorticity oscillations

4.1. *General equations*

In this section, we model the vorticity oscillations, starting from the time evolution of linearized perturbations (Kelvin waves) to the Lamb's vortex. We then derive the first terms of the fully nonlinear time expansion. Finally, we link the two models in a predictor–corrector computation which allows us to recover both the scalings observed in the numerical simulations and the amplification of the oscillation amplitude. In the following, we make use of the observation that viscous diffusion is nearly decoupled from the interaction between the tori and the columnar vortex to employ the inviscid Euler equations.

The velocity and vorticity vectors are decomposed in components related respectively to the central vortex ($v_\theta, \omega_r = -\partial_z v_\theta, r\omega_z = \partial_r(rv_\theta)$) and to the stretching tori ($v_r, v_z, \omega_\theta = \partial_z v_r - \partial_r v_z$). Using incompressibility, the two components v_r and v_z associated with the tori can be written as functions of a streamfunction $\Psi : rv_r = -\partial_z \Psi$, $rv_z = \partial_r \Psi$. Two functions are thus needed to describe the flow evolution: v_θ for the axial vortex and Ψ (or ω_θ) for the tori. Neglecting the advection terms (see equation (3.1)), the dynamics is governed by

$$\frac{\partial v_\theta}{\partial t} = -v_r \omega_z + v_z \omega_r, \tag{4.1}$$

$$\frac{\partial \omega_\theta}{\partial t} = \frac{\partial}{\partial z}\left(\frac{{v_\theta}^2}{r}\right). \tag{4.2}$$

The combination of these equations yields

$$\frac{\partial^2 \omega_\theta}{\partial t^2} = \frac{\partial}{\partial z}\left[\frac{2v_\theta}{r}\frac{\partial v_\theta}{\partial t}\right] = \frac{\partial}{\partial z}\left[\frac{2v_\theta}{r}(-v_r\omega_z + v_z\omega_r)\right]. \tag{4.3}$$

4.2. *Kelvin waves*

We consider small perturbations about the Lamb's vortex,

$$v_\theta^0 = \Gamma\left(\frac{1-\mathrm{e}^{-\alpha r^2}}{r}\right), \quad \omega_z^0 = 2\alpha\Gamma\,\mathrm{e}^{-\alpha r^2}, \quad \omega_r^0 = 0, \tag{4.4}$$

where $2\pi\Gamma$ is the circulation and $1/\alpha^{1/2}$ the vortex core radius. Introducing disturbances of the form: $v_\theta = v_\theta^0 + u_\theta^1$, $\Psi = \Psi^1$, $v_r = u_r^1$, $\omega_\theta = \omega_\theta^1$, we linearize (4.3):

$$\frac{\partial^2 \omega_\theta^1}{\partial t^2} = -\left[\frac{2v_\theta^0}{r^2}\frac{\partial r v_\theta^0}{\partial r}\right]\frac{\partial u_r^1}{\partial z}, \tag{4.5}$$

with the complementary relations

$$u_r^1 = -\frac{1}{r}\frac{\partial}{\partial z}\Psi^1, \quad \omega_\theta^1 = -\frac{1}{r}\frac{\partial^2 \Psi^1}{\partial z^2} - \frac{\partial}{\partial r}\left(\frac{1}{r}\frac{\partial \Psi^1}{\partial r}\right). \tag{4.6}$$

Looking for eigenmodes (which obviously depend on the particular profile v_θ^0), we search for solutions of the form $\Psi^1 = \cos(ft)\sin(K_z z)g(r^2)$. This gives

$$u_r^1 = -K_z\cos(ft)\cos(K_z z)\frac{g(r^2)}{r}, \quad \omega_\theta^1 = \cos(ft)\sin(K_z z)\left[\frac{K_z^2 g(r^2)}{r} - 4rg''(r^2)\right].$$

Substituting these expressions into (4.5), we obtain the equation defining the Kelvin modes of the Lamb's vortex:

$$f^2\left[\frac{K_z^2 g(r^2)}{r} - 4rg''(r^2)\right] = 4\alpha\Gamma^2 K_z^2\left[\frac{\mathrm{e}^{-\alpha r^2}(1-\mathrm{e}^{-\alpha r^2})}{r^2}\right]\frac{g(r^2)}{r}, \tag{4.7}$$

where the angular frequency f for a given axial wavenumber K_z is determined by the boundary condition, $\lim_{r\to\infty} g(r^2) = 0$. To find the dispersion relation, we put (4.7) into a non-dimensional form by making the change of variables $y = K_z^2 r^2$ and defining $G(K_z^2 r^2) = g(r^2)$:

$$\frac{f^2}{\omega_0^2}[G(y) - 4yG''(y)] = \left[\frac{\exp[-(\alpha/K_z^2)y](1-\exp[-(\alpha/K_z^2)y])}{(\alpha/K_z^2)y}\right]G(y). \tag{4.8}$$

Although the vortex turnover time ($1/\omega_0 = 1/2\alpha\Gamma$) is its natural timescale, there is a competition between two lengths, the core radius R_0 and the wavelength: the solution depends on the non-dimensional number $(K_z^2/\alpha)^{1/2} = K_z R_0$. We thus numerically solve (4.8) to determine f/ω_0 as a function of $K_z R_0$, using a shooting method based on a fourth-order Runge–Kutta integration. For a given $K_z R_0$, there exists a multiplicity of modes with different frequencies and different radial structures (see figure 21). We distinguish the different modes by the number n of extrema in the radial profile. For a given wavenumber, the frequency decreases when n increases. Each dispersion relation $f(K_z)$ is approximately linear for small $K_z R_0$. The frequency scales in this limit as

$$f \simeq \frac{0.32}{n}\omega_0 K_z R_0. \tag{4.9}$$

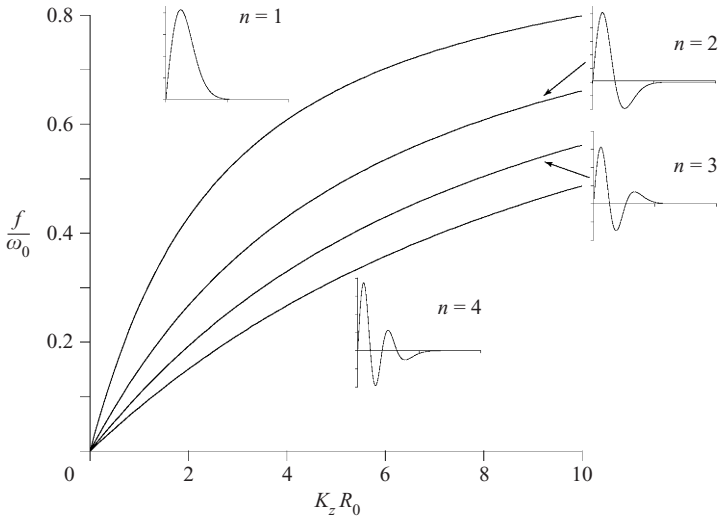

FIGURE 21. Non-dimensional dispersion relation of Kelvin modes and the corresponding radial profiles of azimuthal vorticity numbered by n.

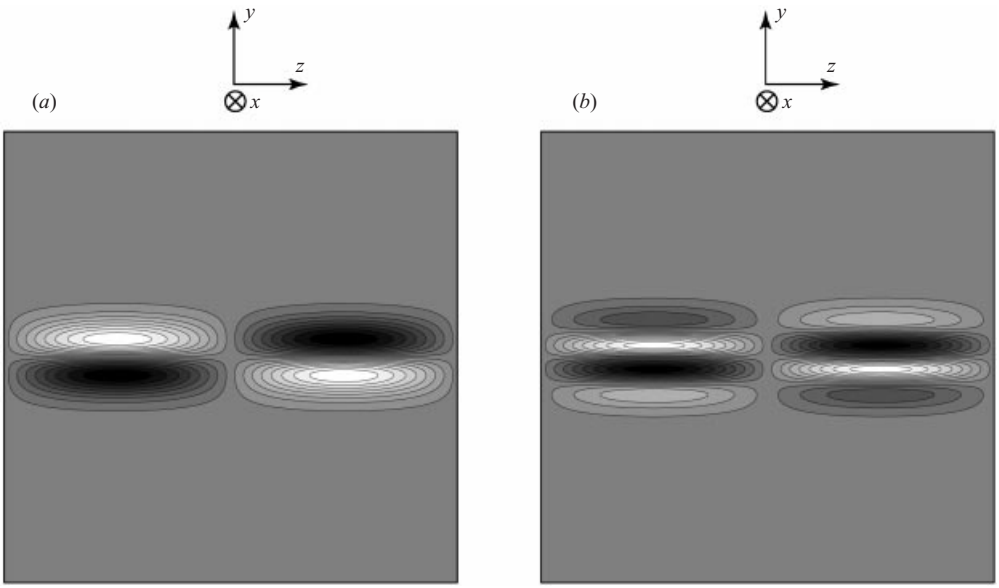

FIGURE 22. Two-dimensional contours of azimuthal vorticity for Kelvin wave eigenmodes in the plane $x = 0$ at equally spaced levels from negative (white) to positive (dark grey) values: (a) mode 1, (b) mode 2.

This is the scaling (3.4) obtained from the numerical simulations. When the wavelength is smaller than the core radius R_0, the propagation becomes strongly dispersive: the angular frequency f tends towards a constant value proportional to the axial vorticity ω_0. Figure 22 shows two-dimensional contours of azimuthal vorticity for the first two modes, for the parameters of the reference run ($\omega_0 = 2.5$, $R_0 = 0.8$, $K_z = 1$). In both cases, the tori are located inside the vortex core. The vortex thus acts as a wave guide for the Kelvin waves.

The shape of these two modes compares rather well with that of the successive

tori observed numerically (figures 8*b* and 11*a*). However, these Kelvin waves are eigenmodes oscillating periodically in time, while in the numerical simulations the tori appear successively and then saturate in amplitude (see figure 16). The initial stretching structure is far from being an eigenmode of (4.7), since it is not located inside the vortex core. It is clear that its decomposition into Kelvin modes can only be a wide wave packet since all the modes are localized inside the vortex core. Moreover, the possibility of such a decomposition is not obvious for any vortex profile v_θ^0, although Arendt *et al.* (1997) have shown that it is possible for a Rankine vortex. The particular temporal dynamics observed also indicates that this decomposition will be difficult. Rather than generalizing the procedure of Arendt *et al.* (1997) for the case under study, figure 16 suggests an interpretation in terms of successive structures interacting with the vortex, more amenable to physical understanding.

4.3. *Direct computation of the reaction tori*

4.3.1. *Radial expression*

A precise way of describing the successive tori is to compute the first terms of the time expansion of the solution, considering now that the initial tori are not perturbative. We start from the Lamb's vortex (4.4) and the stretching tori defined by the stream function: $\Psi^0 = a_0 \sin(K_z z)(1-\exp(-\beta r^2))$. This form mimics the initial rings used in the numerical simulations except that they are localized far from the axis by the Gaussian function. They are characterized by their amplitude a_0 and their radius $1/\beta^{1/2}$, together with the wavenumber K_z along the axis. The velocity and vorticity fields associated with the initial tori are given by

$$\left.\begin{aligned} v_r^0 &= -a_0 K_z \cos(K_z z)\left(\frac{1-\mathrm{e}^{-\beta r^2}}{r}\right), \quad v_z^0 = 2a_0\beta \sin(K_z z)\mathrm{e}^{-\beta r^2}, \\ \omega_\theta^0 &= \frac{a_0 K_z^2}{r}\sin(K_z z)\left[(1-\mathrm{e}^{-\beta r^2}) + \frac{4\beta^2 r^2}{K_z^2}\mathrm{e}^{-\beta r^2}\right]. \end{aligned}\right\} \tag{4.10}$$

We perform a Mac–Laurin expansion of the fields: $v_\theta = v_\theta^0 + t v_\theta^1 + \ldots$, $\Psi = \Psi^0 + t^2\Psi^2 + \ldots$ and $\omega_\theta = \omega_\theta^0 + t^2\omega_\theta^2 + \ldots$. The dynamical equations (4.1) and (4.2) lead to

$$v_\theta^1 = -v_r^0\omega_z^0 + v_z^0\omega_r^0 = -v_r^0\omega_z^0, \quad \omega_\theta^2 = \frac{1}{2}\frac{1}{r}\frac{\partial}{\partial z}(2v_\theta^0 v_\theta^1) \tag{4.11}$$

which gives

$$\omega_\theta^2 = -\left[\frac{v_\theta^0}{r^2}\frac{\partial r v_\theta^0}{\partial r}\right]\frac{\partial v_r^0}{\partial z}. \tag{4.12}$$

This equation is similar to (4.5), except that the response ω_θ^2 is now computed as a function of the initial tori v_r^0:

$$\omega_\theta^2 = -2\alpha\Gamma^2 a_0 K_z^2\left[\frac{\mathrm{e}^{-\alpha r^2}(1-\mathrm{e}^{-\alpha r^2})}{r^2}\right]\sin(K_z z)\left(\frac{1-\mathrm{e}^{-\beta r^2}}{r}\right). \tag{4.13}$$

This correction term ω_θ^2 corresponds to the formation of new tori, with the same variation along the axis ($\sin(K_z z)$) as the initial ones but with opposite sign.

These new tori can be interpreted as a reaction against the initial tori induced by the deformation of the axial vortex. However, they do not have the same radius as the original ones. Being obtained nonlinearly by the multiplication of a function with ω_z^0, they exist only within the axial vortex. The reaction of the vortex is thus

restricted to the inside of the vortex itself, and does not reach the initial tori. As a first approximation, the radius R of the new tori can be computed using the development in r up to r^3 of (4.13):

$$R \sim \frac{1}{(\beta + 3\alpha)^{1/2}}. \tag{4.14}$$

4.3.2. *Characteristic time*

These reaction tori can be seen as created to reduce the deformation of the axial vortex by decreasing its inhomogeneous stretching along the axis. To compute the effective stretching due to these new tori, we have to determine the streamfunction $\Psi^2 = \sin(K_z z)G(K_z^2 r^2)$. We also consider initial tori outside the vortex ($\beta < \alpha$), so that in (4.13) $(1 - \exp(-\beta r^2)) \simeq \beta r^2$. The computation of ω_θ^2 from Ψ^2 leads to

$$[G(y) - 4yG''(y)] = C[\exp[-(\alpha/K_z^2)y](1 - \exp[-(\alpha/K_z^2)y])] \tag{4.15}$$

with the constant $C = -2\alpha\Gamma^2 a_0 \beta$. Noting that $v_z^2 = 2K_z^2 \sin(K_z z)G'(K_z^2 r^2)$, the stretching γ_C at the centre of the box is expanded in time as

$$\gamma_C(t) = 2K_z(a_0\beta + K_z^2 G'(0)t^2 + \ldots). \tag{4.16}$$

This first derivative $G'(0)$ which appears in this equation remains to be expressed using the boundary condition: $\lim_{y\to\infty} G(y) = 0$. We use a numerical shooting method to obtain $G'(0)/C$, as a function of the non-dimensional number $(K_z^2/\alpha)^{1/2} = K_z R_0$. When the wavelength is much smaller than the vortex core radius, $G'(0)$ tends to 0 and it is roughly constant in the limit of small wavenumbers ($K_z R_0 \ll 1$): $G'(0) \simeq 0.17C$. For the parameters of the reference run, the numerical value of $G'(0)$ is around 0.135 so that the stretching vanishes due to the reaction tori at time $t_{1/2}$ given by

$$t_{1/2} \simeq \left(\frac{2}{0.135}\right)^{1/2} \frac{1}{\omega_0 K_z R_0}. \tag{4.17}$$

We recover the scaling observed in the numerical simulations and in §4.2 ($f \sim \omega_0 K_z R_0$), showing that, even if the reaction tori are not eigenmodes of Kelvin waves, they share the same timescale. We get also the prefactor (0.39 in the DNS, see equation (3.4)):

$$f = \frac{\pi}{2t_{1/2}} \simeq 0.41\omega_0 K_z R_0. \tag{4.18}$$

The amplitude of the oscillations in ω_z can be estimated by $\Delta\omega_z/t_{1/2} \simeq \gamma_0\omega_0$ so that

$$\Delta\omega_z \propto \frac{\gamma_0}{K_z R_0}. \tag{4.19}$$

as found in the numerical simulations.

The computation of the first three terms of the Mac–Laurin expansion in time gives good scaling in time and in amplitude. To get a more accurate description of the shape of the reaction tori, we take into account higher-order terms of the expansion in the next section.

4.3.3. *Next order, harmonics*

The next two orders in v_θ and ω_θ are

$$v_\theta^2 = \tfrac{1}{2}(-v_r^0\omega_z^1 + v_z^0\omega_r^1), \quad \omega_\theta^3 = \frac{1}{3}\frac{1}{r}\frac{\partial}{\partial z}(v_\theta^{1^2} + 2v_\theta^0 v_\theta^2).$$

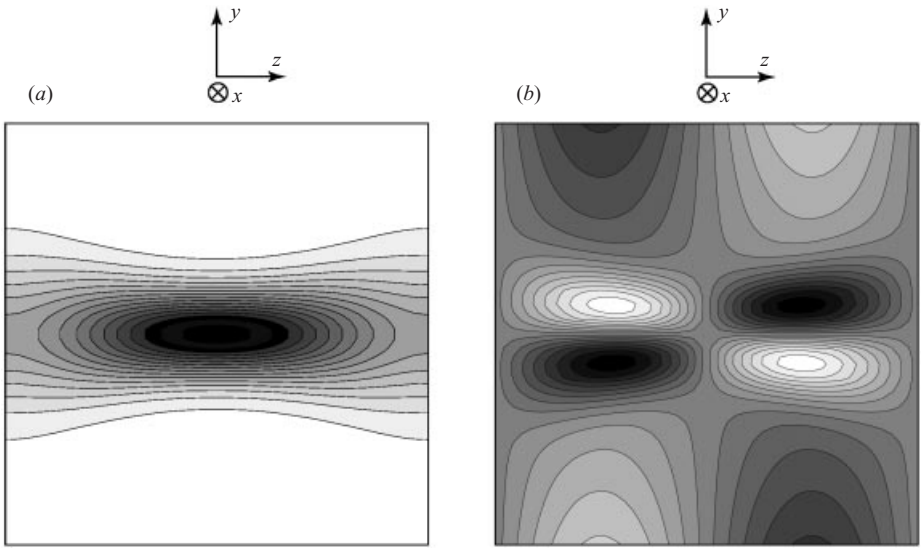

FIGURE 23. Two-dimensional contours in the plane $x = 0$ at equally spaced levels from the minimum in white to the maximum in dark grey: (a) of axial vorticity ω_z at time $t_{1/2}$, (b) of vorticity ω_θ normal to the plane $x = 0$ at time t_1. The development of the solution to the third order in time allows us not only to predict the scaling in time but also to reproduce the conical shape of the reaction tori.

Since the reaction tori appear inside the vortex, we can develop Ψ^0 to the first order in βr^2. This leads to

$$\left.\begin{aligned} v_\theta^2 &\approx \alpha\Gamma {a_0}^2\beta^2 K_z^2\{2 - \alpha r^2[1 + \cos(2K_z z)]\}r\mathrm{e}^{-\alpha r^2}, \\ \omega_\theta^3 &\approx -\tfrac{4}{3}\alpha^2{\Gamma}^2{a_0}^2\beta^2 K_z^3 \sin(2K_z z)\{2\mathrm{e}^{-\alpha r^2} - 1\}r\mathrm{e}^{-\alpha r^2}. \end{aligned}\right\} \tag{4.20}$$

We compute the axial vorticity ω_z at time $t_{1/2}$ and the vorticity ω_θ at time t_1 by resumming the first three terms of the expansion. The corresponding iso-contours are plotted in figure 23, using the reference parameters. Note the nearly perfect similarity with, respectively, figure 7 and figure 8(b). From the quadratic expression (4.1) and (4.2), it can be seen that the successive terms in the expansion correspond to higher and higher development in the $K_z z$ harmonics (each term v_θ^n and ω_θ^{n+1} containing all the odd/even harmonics (with the cos/sin phase respectively) up to nK_z). These harmonics are responsible for the conical shape of each torus (see figures 14, 23).

The previous calculation gives the shape and the short time evolution of the reaction tori (roughly up to $t_{1/2}$). To obtain the saturation of the reaction, we should compute the next-order terms (v_θ^3 and ω_θ^4). This is a tedious calculation, in particular because of the harmonics. To model the saturation of the reaction tori, we instead prefer to develop a physical description based on both structures and waves.

4.4. *Saturation of the reaction tori*

The dynamics of the reaction tori can be approximated by a predictor–corrector method. We initially guess the temporal evolution of the tori and deduce the modulation of the vortex under the effect of stretching. We can then compute the reaction tori induced by the vortex, thus obtaining a better estimate of the stretching structures. Ideally, this algorithm should be repeated: knowing the evolution of the tori,

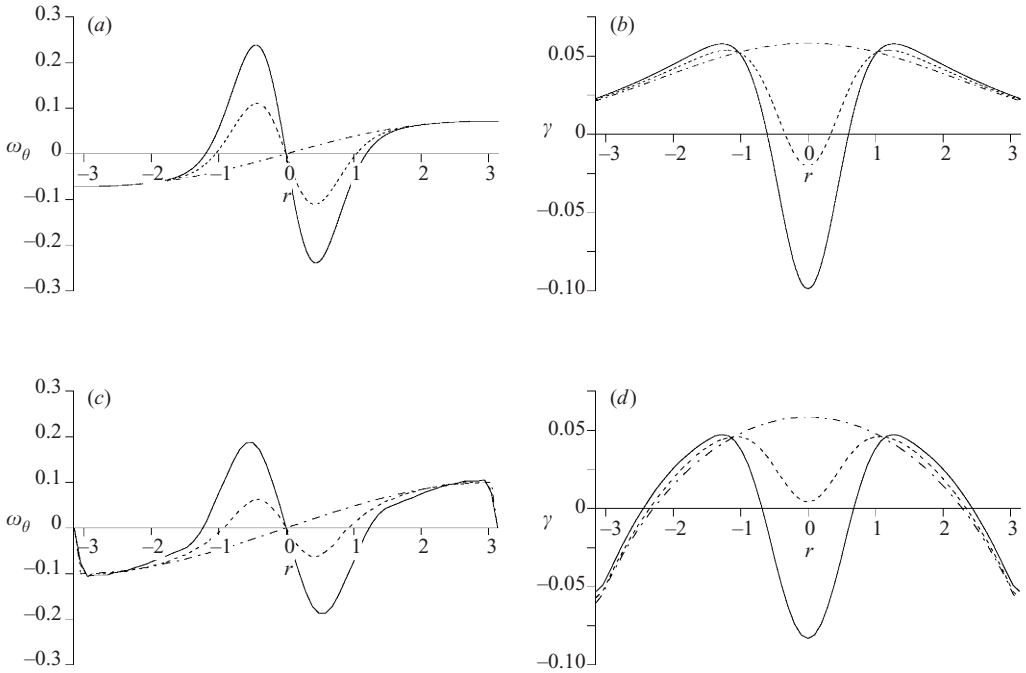

FIGURE 24. Amplification model and numerical results for the reference case: radial variation for $K_z z = \pi/2$ of: (*a*) ω_θ at the initial time (dot-dashed line), at times $t_{1/2}$ (dashed line) and at t_1 (solid line) to be compared with numerical ones on (*c*); (*b*) γ at the initial time (dot-dashed line), at times $t_{1/2}$ (dashed line) and at t_1 (solid line) to be compared with numerical ones on (*d*).

we should compute again the deformation, and then a better approximation of the deformation and so on.

The external tori do not oscillate in time but successive structures are induced one inside the others. On the other hand, the vortex is modulated in time as if it were subjected to an oscillating stretching. We can thus take as an initial guess tori oscillating in time: $\tilde{\Psi}^0 = \cos(ft)\sin(K_z z)g^0(r^2)$, where g^0 is given by the initial condition $g^0(r^2) = a_0(1 - \exp(-\beta r^2))$ and where the oscillation angular frequency f is derived from the previous computation. This stretching structure induces a deformation of the vortex computed using (4.1):

$$v_\theta = v_\theta^0 + \frac{2\alpha\Gamma K_z}{f}\sin(ft)\cos(K_z z)\frac{g^0(r^2)\mathrm{e}^{-\alpha r^2}}{r}. \tag{4.21}$$

Knowing the evolution of the deformation, we replace the initial guess in which the oscillation in time was imposed by a more accurate expression for the initial tori and the reaction tori:

$$\Psi = \sin(K_z z)g^0(r^2) + \sin(K_z z)(\cos(ft) - 1)g^2(r^2). \tag{4.22}$$

Inserting these expressions in (4.3) gives

$$\left[\frac{K_z^2 g^2(r^2)}{r} - 4rg^{2\prime\prime}(r^2)\right] = \frac{4\alpha\Gamma^2 K_z^2}{f^2}\left[\frac{\mathrm{e}^{-\alpha r^2}(1 - \mathrm{e}^{-\alpha r^2})}{r^2}\right]\left(\frac{1 - \mathrm{e}^{-\beta r^2}}{r}\right). \tag{4.23}$$

Equation (4.23) is solved by shooting to determine the derivative of g^2 on the axis.

The solutions are presented on figure 24 at times t_0, $t_{1/2}$ and t_1, for the parameters of the reference case. The radial profile of azimuthal vorticity shows that the reaction tori are localized near the axis whereas the initial rings (dot-dashed line) are far from it. More important, the initial tori are still visible at t_1 and remain unaffected by the secondary ones. This is the case in the numerical simulations (figure 16) and shows a first advantage of this model based on structures over Kelvin modes. The discrepancy in figure 24 between the numerical simulations and the model essentially comes from the different localizations of the initial tori. The second striking feature is that the stretching in the vortex core is not only reversed at $t = t_1$ but is also amplified. The amplification factor between $t = 0$ and $t = t_1$ is 1.69 compared to 1.75 in the reference run (figure 6). The predictor–corrector method nonetheless allows us to recover the scaling in time and also explains the amplification in the oscillation amplitude: the reaction cannot occur far from the axis but only near the core radius so that the vortex response overshoots.

5. Discussion and conclusion

In this paper, we have studied the evolution of a vortex subjected to a non-uniform stretching induced by vortex rings localized far from its core. We find that the vortex, deformed by this stretching, reacts by inducing secondary tori-shaped structures which screen the effect of the primary ones. This vortex feedback does not match the perturbation, the structures being induced closer to the vortex than the initial ones and with an increased amplitude. It turns out that the interaction between the vortex and the surrounding stretching structures follows neither a Burgers-like behaviour (constant stretching) nor that of Kelvin modes (perfect oscillation) but is an overshooting reaction.

Subsequently, there is a secondary reaction against the first one, which leads to oscillations of the axial vorticity in a repetitive process. However, these amplified oscillations are not observed to persist indefinitely in the simulations, even when the viscous damping is negligible. This is due to the emergence of spatial harmonics along the axis (in $K_z z$) which are generated by the nonlinear vortex–stretching interaction (see equation (4.20) in § 4.3.3). These nonlinearities grow in time and create structures of smaller periodicity in z which will eventually disrupt the above oscillations.

The characteristic frequency of the oscillations scales as $\omega_0 R_0 K_z$, like that of Kelvin modes in the limit of small wavenumbers K_z. However, Kelvin waves correspond to simple oscillations of both the axial and the azimuthal vorticity inside the vortex, unlike what is observed in the numerical simulations: the first reaction tori do not oscillate, but rather saturate in amplitude (figure 16). This suggests an alternative interpretation in terms of successive reaction tori of smaller radius and opposite sign embedded in the previous ones. We proposed two models based on this structural approach. A precise expansion in time of the fully nonlinear solution was derived. It gives an expression for both the oscillation frequency and the shape of the reaction tori, including the harmonics. Using this frequency, we constructed a predictor–corrector estimate of the interaction between stretching and rotation, which allows us to recover not only the shape of the reaction structures but also their increasing oscillation amplitude. This particular problem thus shows that it could be more interesting to investigate the interaction between stretching and vorticity in terms of structures (the initial tori and successive reaction ones), rather than in terms of waves. The appearance of smaller and smaller structures seems to be a robust mechanism which could be linked to the dynamics of vortex breakdown.

We have proved that there is a feedback of the vortex on the stretching. The mechanism is mainly that of Ekman pumping: the stretching being inhomogeneous, it induces variations of the vortex rotation along its axis. The pressure gradient can no longer balance the centrifugal force, the latter having a solenoidal part. A secondary flow is thus induced, which stretches the vortex at the places where it was slowly rotating and compresses it where it was rotating fast. Globally, the vortex tends to reduce the stretching to which it is subjected, as soon as the stretching is localized in space. Surprisingly, this basic mechanism has not been considered before even though it is at the origin of the propagation of Kelvin waves (Kelvin 1880), of the core dynamics (Melander & Hussain 1994), of the Rayleigh stability criterion, etc. We have shown here that the negative feedback of rotation on stretching is a more general mechanism which can be understood independently of the particular situations and formalisms in which it occurs. This point can be discussed by comparing the natural timescales of the problem: $\tau_{stretching} = 1/\gamma_0$ characterising the stretching and $\tau_{feedback} = 1/\omega_0 R_0 K_z$ measuring the reaction timescale. The ratio of the two is then given by

$$B = \omega_0 R_0 / \gamma_0 R_\gamma \tag{5.1}$$

where R_γ holds for the characteristic length over which the stretching is inhomogeneous. This non-dimensional parameter B characterizes the relative importance of the feedback mechanism and of the stretching process. For small B, $\tau_{feedback} \gg \tau_{stretching}$ so that the reaction can be neglected. In the limit case of homogeneous stretching (Burgers-like models), R_γ tends to infinity and B tends to zero: there is strictly no reaction. On the other hand, if $B \gg 1$, the negative feedback of rotation on stretching must play a crucial role. This is true, even for quite small B: for our reference run, B is equal to 4.82; the first stages of a similar dynamics can be observed in Marshall (1997), at a compressive stagnation point, for $B = 1.06$.

Thus, Burgers-like models (Burgers 1940; Sullivan 1959; Donaldson & Sullivan 1960; Bellamy-Knights 1970; Neu 1984; Craik & Criminale 1986; Moffatt *et al.* 1994; Kerr & Dold 1994; Verzicco *et al.* 1995; Le Dizès *et al.* 1996; Gibbon *et al.* 1999) capture well the vortex dynamics if B is much smaller than 1. This corresponds to the situation where the typical velocity associated with the stretching $\gamma_0 R_\gamma$ is much larger than the rotation speed $\omega_0 R_0$, that is to say, when there is no vortex but a nearly pure strain region. As soon as the rotation becomes important compared to the stretching, the reaction of rotation on stretching becomes an essential part of the dynamics.

The authors would like to acknowledge Professor Yves Couder for fruitful discussions. The computations were carried out on the 90/8 Cray computer of the Institut du Développement et des Ressources en Informatique Scientifique.

REFERENCES

Abid, M. & Brachet, M. 1998 Direct numerical simulations of the Bachelor training vortex by a spectral method. *Phys. Fluids* **10**, 469–475.

Andreotti, B. 1999 Action et réaction entre étirement et rotation, du laminaire au turbulent. PhD Thesis, Université Paris 7, Paris.

Andreotti B., Douady, S. & Couder, Y. 1997 About the interaction between vorticity and stretching in coherent structures. In *Turbulence Modelling and Vortex Dynamics* (ed. O. Boratav & A. Erzan), pp. 92–108. Springer.

Arendt, S., Fritts, D. C. & Andreassen, O. 1997 The initial value problem for Kelvin vortex waves. *J. Fluid Mech.* **344**, 181–212.

Belin, F., Maurer, J., Tabeling, P. & Willaime, H. 1996 Observation of worms in fully developed turbulence. *J. Phys. Paris* II **6**, 573–583.

Bellamy-Knights, P. G. 1970 An unsteady two-cell vortex solution of the Navier-Stokes equations. *J. Fluid Mech.* **41**, 673–687.

Brachet, M. E. 1990 Géométrie des structures à petite échelle dans le vortex de Taylor-Green. *C. R. Acad. Sci.* II **311**, 775.

Brachet, M. E., Meiron, D. I., Orszag, S. A., Nickel, B. G., Morf, R. H. & Frisch, U. 1983 Small-scale structure of the Taylor–Green vortex. *J. Fluid Mech.* **130**, 411–452.

Burgers, J. M. 1940 Application of a model system to illustrate some points of the statistical theory of free turbulence. *Proc. Acad. Sci. Amsterdam* **43**, 2–12.

Cadot, O., Douady, S. & Couder, Y. 1995 Characterisation of the low-pressure filaments in a three dimensional turbulent shear flow. *Phys. Fluids* **7**, 630–646.

Craik A. D. D. & Criminale W. O. 1986 Evolution of wavelike disturbances in shear flows: a class of exact solution of Navier-Stokes equations. *Proc. R. Soc. Lond.* A **406**, 13–26

Da Rios, L. S. 1906 Sul Moto d'un liquido indefinito con un filetto vorticoso di forma qualunque. *Rend. Circ. Mat. Palermo.* **22**, 117–135.

Donaldson, C. D. & Sullivan, R. D. 1960 Behaviour of solutions of the Navier-Stokes equations for a complete class of three-dimensional viscous vortices. In *Proc. Heat Transfer & Fluid Mech. Inst.*, Stanford University.

Douady, S., Couder, Y. & Brachet, M. E. 1991 Direct observation of the intermittency of intense vorticity filaments in turbulence. *Phys. Rev. Lett.* **67**, 983–986.

Gibbon, J. D., Fokas, A. S. & Doering, C. R. 1999 Dynamically stretched vortices as solutions of the 3D Navier-Stokes equations. *Physica* D **132**, 497–510.

Gottlieb, D. & Orszag, S. A. 1977 *Numerical Analysis of Spectral Methods: Theory and Applications.* SIAM, Philadelphia.

Hasimoto, H. 1972 A soliton on a vortex filament. *J. Fluid Mech.* **51**, 477–485.

Hopfinger, E. 1992 *Rotating Fluids in Geophysical and Industrial Applications.* CISM Courses and Lectures 329. Springer.

Hussain, F. 1986 Coherent structures and turbulence. *J. Fluid Mech.* **73**, 303–356.

Jeong, J. & Hussain, F. 1995 On the identification of a vortex. *J. Fluid Mech.* **285**, 69–94.

Jimenez, J. & Wray, A. A. 1994 Columnar vortices in isotropic turbulence. *Meccanica* **4**, 453–464.

Jimenez, J., Wray, A. A., Saffman, P. G. & Rogallo, R. S. 1993 The structure of intense vorticity in homogeneous isotropic turbulence. *J. Fluid Mech.* **255**, 65–90.

Kelvin Lord 1880 Vibrations of a columnar vortex. *Phil. Mag.* **10**, 155–168.

Kerr, O. S. & Dold, J. W. 1994 Periodic steady vortices in a stagnation-point flow. *J. Fluid Mech.* **276**, 307–325.

Le Dizès, S., Rossi, M. & Moffatt, H. K. 1996 On the three-dimensional instability of elliptical vortex subjected to stretching. *Phys. Fluids* **8**, 2084–2090.

Leonard, A. 1994 Nonlocal theory of area-varying waves on axisymmetric vortex tubes. *Phys. Fluids* **6**, 765–777.

Marshall, J. S. 1997 The flow induced by periodic vortex rings wrapped around a columnar vortex core. *J. Fluid Mech.* **345**, 1–30.

Maxworthy, T., Hopfinger, E. J. & Redekopp, L. G. 1985 Wave motions on vortex cores. *J. Fluid Mech.* **151**, 141–165.

Melander, M. V. & Hussain, F. 1993 Polarised vorticity dynamics on a vortex column. *Phys. Fluids* **5**, 1992–2003.

Melander, M. V. & Hussain, F. 1994 Core dynamics on a vortex column. *Fluid Dyn. Res.* **13**, 1–37.

Miura, H. & Kida, S. 1997 Identification of tubular vortices in turbulence. *J. Phys. Soc. Japan* **66**, 1331–1334.

Moffatt, H. K., Kida, S. & Ohkitani, K. 1994 Stretched vortices – the sinews of turbulence; large Reynolds number asymptotics. *J. Fluid Mech.* **259**, 241–264.

Neu, J. C. 1984 The dynamics of stretched vortices. *J. Fluid Mech.* **143**, 253–276.

Ohkitani, K. & Kishiba, S. 1995 Nonlocal nature of vortex stretching in an inviscid fluid. *Phys. Fluids* **7**, 411–421.

Ricca, R. L. 1994 The effect of torsion on the motion of a helical vortex filament. *J. Fluid Mech.* **273**, 241–259.

Saffman, P. G. 1992 *Vortex Dynamics*. Cambridge University Press.

Samuels, D. C. 1998 A finite length instability of vortex tubes. *Eur. J. Mech.* B **17**, 587–594.

Schoppa, W., Hussain, F. & Metcalfe, R. W. 1995 A new mechanism of small scale transition in a plane mixing layer: core dynamics of spanwise vortices. *J. Fluid Mech.* **298**, 23–80.

Siggia, E. D. 1981 Numerical study of small scale intermittency in three-dimensional turbulence. *J. Fluid Mech.* **107**, 375–406.

Sullivan, R. D. 1959 A two-cell vortex solution of the Navier-Stokes equations. *J. Aero/Space Sci.* **26**, 767–772.

Taylor G. I. 1938 Production and dissipation of vorticity in a turbulent fluid. *Proc. R. Soc. Lond.* A **164**, 15–23.

Tsinober, A. 1998 Is concentrated vorticity that important? *Eur. J. Mech.* B **17**, 421–449.

Verzicco, R., Jimenez, J. & Orlandi, P. 1995 On steady columnar vortices under local compression. *J. Fluid Mech.* **299**, 367–388.